

Article

Photocatalytic Evaluation of TiO_x Films Produced by Cathodic Arc-PVD with Silver Addition by UVC Photo-Reduction Method

Alma Yunuen Raya-Tapia ¹, Francisco Ung-Medina ², Guillermo César Mondragón-Rodríguez ³,
Eric Mauricio Rivera-Muñoz ⁴, José Apolinar-Cortés ¹, Franklin J. Méndez ⁵ and Rafael Huirache-Acuña ^{1,*}

¹ Facultad de Ingeniería Química, Universidad Michoacana de San Nicolás de Hidalgo, Francisco J. Múgica S/N, Ciudad Universitaria, Morelia 58060, Mexico

² Potabilization Department, Water, Sewerage and Sanitation Operator Organization of Morelia, OOAPAS, OOAPAS, C. Manuel Carpio No.66, Morelia 58096, Mexico

³ Conacyt, Center for Engineering and Industrial Development, CIDESI, Av. Playa Pie de la Cuesta No. 702, Desarrollo San Pablo, Santiago de Querétaro, Querétaro 76125, Mexico

⁴ Centro de Física Aplicada y Tecnología Avanzada, Departamento de Nanotecnología, Universidad Nacional Autónoma de México, A.P. 1-1010, Santiago de Querétaro 76000, Mexico

⁵ Centro de Investigación en Ciencia Aplicada y Tecnología Avanzada, CICATA Morelos, Instituto Politécnico Nacional, Boulevard de la Tecnología 1036 Z-1 P 2/2, Atlacholoaya 62790, Mexico

* Correspondence: rafael.huirache@umich.mx



Citation: Raya-Tapia, A.Y.; Ung-Medina, F.; Mondragón-Rodríguez, G.C.; Rivera-Muñoz, E.M.; Apolinar-Cortés, J.; Méndez, F.J.; Huirache-Acuña, R. Photocatalytic Evaluation of TiO_x Films Produced by Cathodic Arc-PVD with Silver Addition by UVC Photo-Reduction Method. *Inorganics* **2022**, *10*, 148. <https://doi.org/10.3390/inorganics10100148>

Academic Editors: Alejandro Pérez-Larios and Oomman K. Varghese

Received: 10 August 2022

Accepted: 14 September 2022

Published: 21 September 2022

Publisher's Note: MDPI stays neutral with regard to jurisdictional claims in published maps and institutional affiliations.



Copyright: © 2022 by the authors. Licensee MDPI, Basel, Switzerland. This article is an open access article distributed under the terms and conditions of the Creative Commons Attribution (CC BY) license (<https://creativecommons.org/licenses/by/4.0/>).

Abstract: A titanium (Ti) commercial cathode material and high purity Ar and O₂ were used in the cathodic arc physical vapor deposition (arc-PVD) process. The TiO_x coating was deposited on the three sets of Raschig rings using decreasing ratios of Ar/O₂:440/60, 400/100 and 300/100. The cross sections of the TiO_x PVD coating were analyzed using field emission scanning electron microscopy (FE-SEM), X-ray energy dispersive spectroscopy (EDS), and X-ray diffraction (XRD). A homogeneous layer of Ti with small O content was observed, and the data suggest that a thin TiO_x oxide film was deposited. For this reason, a thermal treatment was applied to the coating to oxidize it and form the rutile phase of TiO₂ in the coating, which was demonstrated by grazing incidence XRD. In addition, the TiO_x coatings absorb radiation, which was observed by diffuse reflectance band gap energy measurement. Silver (Ag) was added by the photo-reduction method, using UVC light to activate the TiO₂ coating, and the band gap energy was analyzed by diffuse reflectance. The photocatalytic activities of the films were evaluated by degradation of the model dye rhodamine B and in the removal of fecal coliforms using two matrices, water from a secondary treatment effluent, and synthetic water.

Keywords: films; physical vapor deposition; rhodamine B; degradation; photo-catalysis; fecal coliforms

1. Introduction

Titanium dioxide (TiO₂) is a wide bandgap semiconductor available in the form of three crystalline polymorphs: rutile (tetragonal), anatase (tetragonal), and brookite (orthorhombic). TiO₂ is a widely studied material due to its very attractive physical properties, such as long-term stability, oxidative ability, wide indirect band gap [1], low cost and low biological toxicity. These qualities make it a promising material for photoelectric applications, such as semiconductor electrodes in solar cells [2], photo-catalysis [3], sensors [4], adsorption [5], biosensors [6–8], cancer therapy [9,10], and UV detectors [11,12].

Thin film materials are practical and attracted extensive interdisciplinary research interests between physics, chemistry, and electronics [13,14]. A functional material in the form of a porous film solidly bonded to cheap substrates (steel or polymers) allows it to function effectively and practically, this is important particularly for large-scale industrial applications. Numerous applications involve, for example, optical films for dye-sensitized

solar cells [15], as electrodes in electrochemistry [16], photo-electrocatalysis [17], and photocatalysis [18], and many others [19].

A large number of processing techniques were developed for the deposition of TiO₂ films. TiO₂ thick films are fabricated by a colloidal processing route (e.g., electrophoretic deposition) [20,21] and hydrothermal methods [22,23]. Sol-gel processing is also used to fabricate TiO₂ thin films [24–26], however, it presents film cracking and peeling [27], and there is also a thickness limitation for each layer (~1 μm). Several vapor processing techniques, (i.e., sputtering [28,29]), chemical vapor deposition [30–32], spray pyrolysis [33,34], and physical vapor deposition (PVD) [35,36]), were applied to fabricate TiO₂ thin films.

The PVD refers to the processes of deposition of thin films and nanostructures through evaporation of solid precursors in their vapor phase by physical approaches, followed by condensation of the vapor phase on substrates. The whole process consists of three stages: (1) evaporation of the solid source, (2) vapor phase transport from the source to the substrates, and (3) vapor condensation on the substrates [37]. Common PVD techniques include laser ablation [38,39], sputtering [40,41], and cathodic arc [42–45]. In the PVD techniques the structure of TiO₂ films and their properties depend on the deposition method and on the substrate temperatures during film growth and the energy of the ions involved.

In the last two decades, great progress was achieved in various applications of TiO₂, however, within the TiO₂ structure the photo-excited electrons and holes rapidly recombine, thus diminishing the effectiveness of photo-catalysis [46]. Several approaches were proposed to amend these difficulties; one of the effective modifications is the doping with noble metals in TiO₂, where hetero-structures and new interfaces are formed that improve the photo-catalytic efficiency. Localized surface plasmon resonance (LSPR) on noble metal surfaces, which arises from the collective oscillations of electrons near them, enhances the interaction between catalysts and light, and is explained as the mechanism responsible for affecting the photo-catalytic efficiency [47]. So far, Pt [48], Au [49], Ag [50], and Cu [51], were added to TiO₂. Among the metals, Ag is widely used because it is comparatively cheap, showing a suitable work function.

In particular, heterogeneous catalysis using TiO₂ as a photocatalyst is an attractive method for the decomposition of various undesirable pollutants [52,53]. As persistent organic pollutants (POPs) are a group of highly toxic chemicals for humans and the environment, several governments in the world signed the Stockholm Convention, which came into force in 2004 and established the elimination of twelve priority POPs [54]. Some examples of these POP-type compounds are pesticides, herbicides, toxic dyes used in the textile industry, and organochlorine insecticides, among others. Organic dyes require special attention, as they are shown to be highly water soluble, toxic, carcinogenic, and mutagenic to humans, animals, and aquatic life [55]. The textile industry in its process uses dyes with complex and persistent structures, such as rhodamine B (RhB), which is a cationic dye of the xanthene class, highly soluble in water, and widely used as a textile dye and in food products. It is also a well-known fluorescent tracer and biomarker [56–59]. Due to its wide use, its degradation mechanism was studied previously; the degradation products are known [60,61] and can be easily followed by spectrophotometry.

The concentration of toxic materials and infectious microorganisms in the natural resources of drinking water is constantly increasing, causing severe environmental pollution. The traditional chemical methods for the disinfection of drinking water have limitations due to their costs for undeveloped nations. Furthermore, a generation of harmful disinfection byproducts associated with the chemical disinfection processes, such as chlorination, is a source of rising concern [62]. Table 1 shows some works on dye degradation and disinfection by photocatalysis using TiO₂ and TiO₂ with Ag.

Table 1. Research on dye degradation and disinfection by photocatalysis.

Photocatalyst	Pollutant	Pollutant Concentration	Reaction Time and Type of Irradiation	Results
Ag-doped TiO ₂ thin films using a modified sol-gel method and photo-chemical deposition [24]	Rhodamine B (RhB)	10 mL of RhB solution with initial concentration of 10 ⁻⁴ mol ⁻¹	90 min, UV lamp (400 W)	Degradation efficiency from 38% to 90%.
Fe- or Ag-doped TiO ₂ -MWCNT nanocomposite thin films by sol-gel drop coating method [63]	Methylene blue (MB)	200 mL of MB solution with initial concentration of 5 × 10 ⁻⁶ M	240 min, visible-light (200 W)	Degradation efficiency from 40.39% to 58.27%. k _{ap} = 0.002 and 0.003 min ⁻¹
Ag/TiO ₂ films by hybrid sol-gel method [64]	Methyl orange (MO)	100 mL of MO solution with initial concentration of 5 × 10 ⁻⁵ mol/L	60 min, UV lamp (1000 W)	K _{ap} = 0.0014 min ⁻¹
Synthesis of Ag/TiO ₂ nanocomposites immobilized by Dip-coating on borosilicate glass [65]	Methyl orange (MO)	125 mL of MO solution with initial concentration of 10 ppm at a fixed pH (7.0)	5.5 h, UV lamp (100 W)	Degradation efficiency from 59.5% to 75.8%. k _{ap} = 0.003 min ⁻¹
Ag-TiO ₂ composite thin films deposited on glass slides by sol-gel spin coating technique [66]	<i>Escherichia coli</i>	10 mL <i>E. coli</i> solution with initial concentration of 4.46 × 10 ⁸ CFU/mL	80 s, UV-C lamp (15 W)	Bacterial elimination 94%
Atomic layer deposited anatase-TiO ₂ thin films on rutile-TiO ₂ nanotubes [67]	<i>Escherichia coli</i>	~10 ⁶ CFU mL ⁻¹	120 min, UV-A lamp	Bacterial elimination 40%

For such reasons in this research, a series of TiO₂ coatings was synthesized by the cathodic arc-PVD deposition method on commercial borosilicate Raschig rings (Morelia, Mexico). The effect of the O flow during deposition on the TiO_x characteristics was analyzed. A thermal treatment is explored to increase the amount of oxygen on the surface of the coating, and Ag was added into the film by the photo-reduction method under UVC light. The photo-catalytic activity of these TiO_x PVD functional coatings is evaluated in model reactions.

2. Results

2.1. Characterization of the TiO_x Arc-PVD Coatings in the As-Coated State

2.1.1. X-ray Diffraction (XRD)

Crystalline phase identification was performed by comparing the 2θ angular positions obtained in the XRD patterns with the diffraction standards from the database, using the PANalytical X'Pert HighScore program. For phase identification, the arc-PVD TiO_x coatings were also deposited in silicon (Si) oriented in the (100) direction. Figure 1a displays the diffraction pattern of the Si wafer, while the diffraction patterns in Figure 1b correspond to the TiO_x coatings with Ar/O₂ flow ratios of 300/100, 400/100 and 440/60. The TiO_x coatings display a reflection peak at 2θ ≈ 38°, and it is observed that the peak intensity decreases as the O₂-flow increases. However, no signs of any oxidation were detected after the XRD analysis of the TiO_x in the as-coated state.

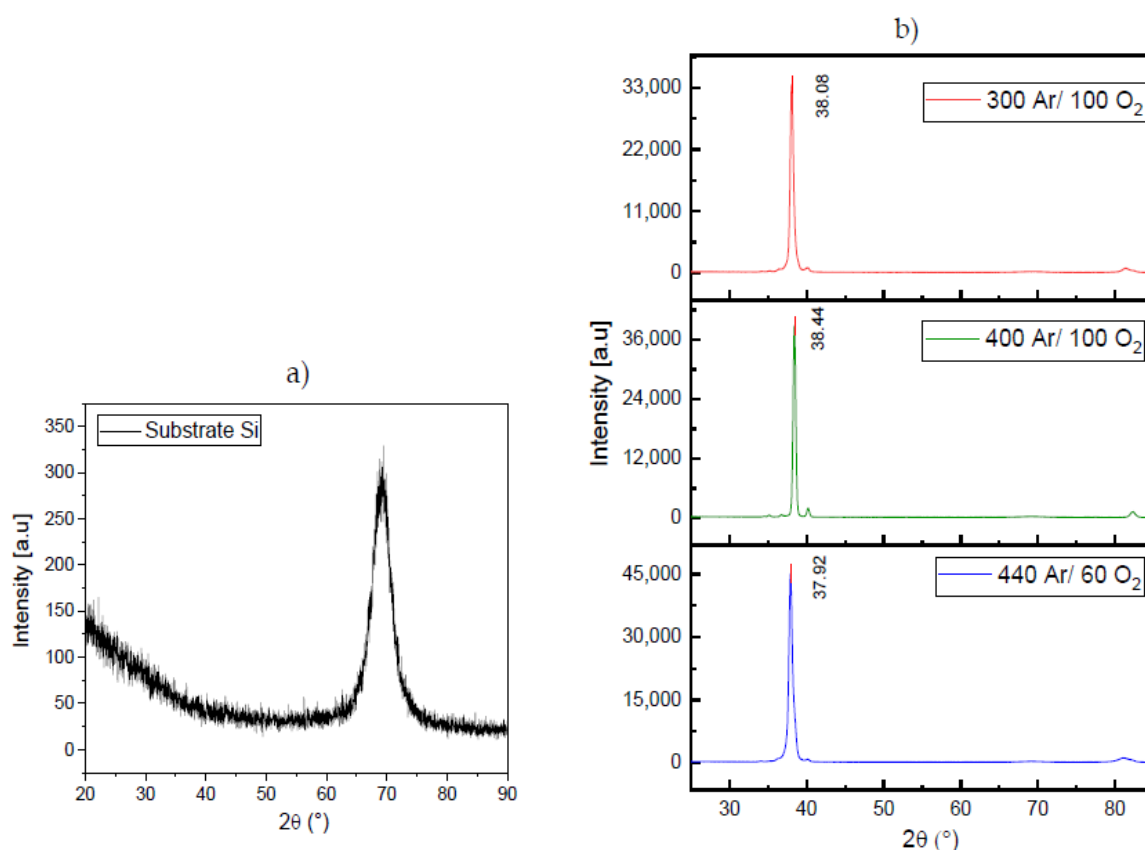


Figure 1. X-ray diffraction patterns of (a) silicon substrate and (b) TiO_x arc-PVD coatings deposited using different Ar/ O_2 flow ratios.

The diffraction patterns display peaks of pure Ti α -phase, which has a compact hexagonal structure (ICCD File 00-044-1294). Table 2 shows the crystallographic planes of Ti α with their corresponding 2θ angle, which is in agreement with the diffraction peaks of the TiO_x coatings.

Table 2. Crystalline planes corresponding to Ti in α -phase.

Ti α		
2θ Angle	hkl Plane	Intensity [a.u.]
35.094	(100)	315.3
38.422	(002)	36,126.04
40.171	(101)	1690.58
53.005	(102)	20.89
77.37	(201)	20.24
82.292	(004)	1033.52

2.1.2. Scanning Electron Microscopy (SEM)

Figure 2 shows images obtained by FE-SEM of the cross sections of the arc-PVD TiO_x coatings with different Ar/ O_2 flow ratio. Each of the micrographs shows the relatively homogeneous TiO_x coatings deposited on the Si substrates. The thickness of each coating was measured by the SEM, giving a thickness of $\sim 1.33 \mu\text{m}$ for the flow of 440 Ar/60 O_2 , $\sim 1.18 \mu\text{m}$ for 400 Ar/100 O_2 , and $\sim 1.20 \mu\text{m}$ for 300 Ar/100 O_2 . There is a slight decrease in the deposition rate upon the raise of O_2 during deposition. This is explained by the increased oxidation of the Ti-target material with O, which makes the evaporation process difficult, thus slightly decreasing the deposition rate. The images show a uniform granular surface and the presence of some macro- or micro-droplets of various sizes, which are

typical of the arc deposition method. These coating features might be deposited at the beginning of the process, thus affecting the whole local morphology of the further TiO_x layer; see left SEM-image in Figure 2c.

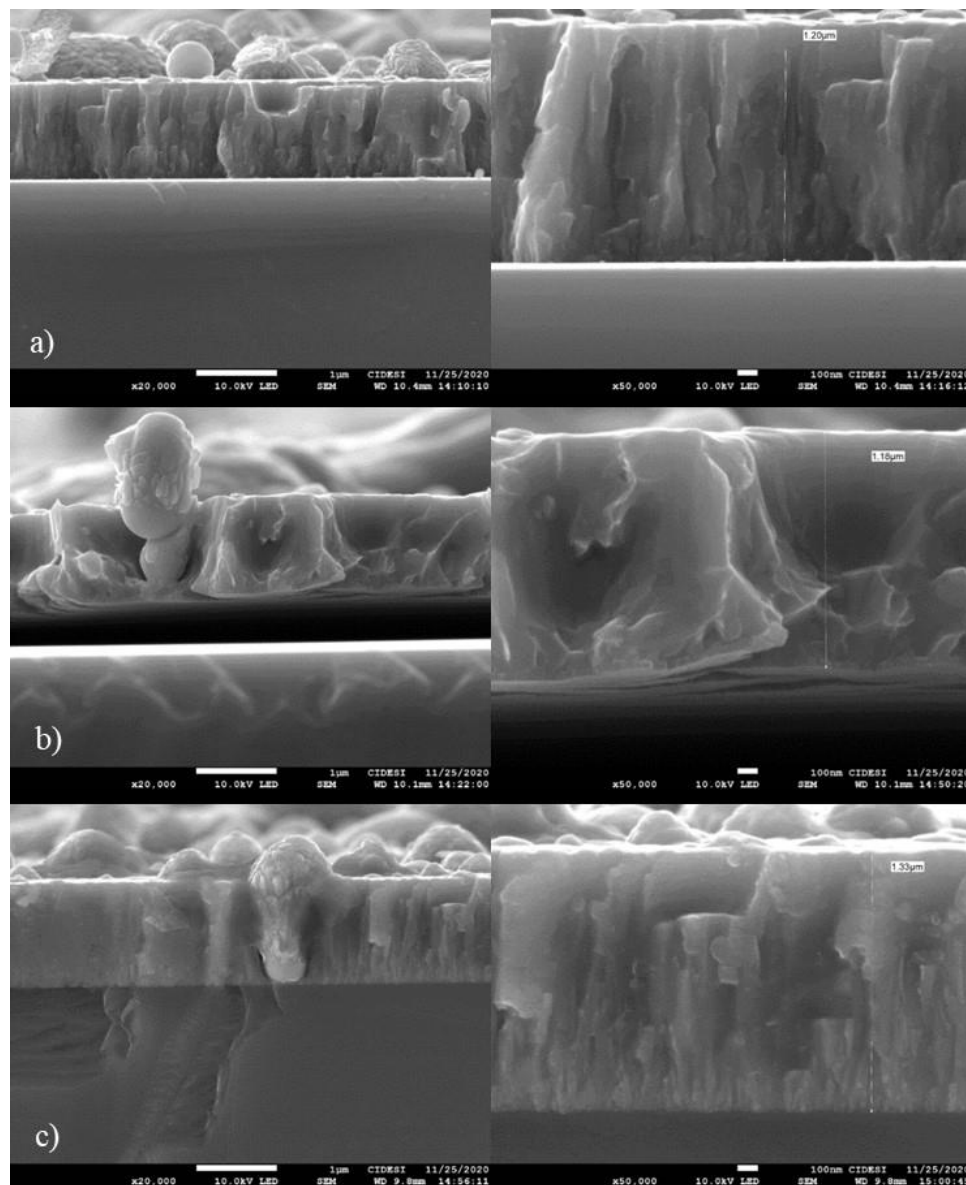


Figure 2. FE-SEM micrographs of the cross sections of the arc-PVD TiO_x coating with Ar and O_2 flow ratios of (a) 300/100, (b) 400/100, and (c) 440/60.

2.1.3. X-ray Energy Dispersive Spectroscopy (EDS)

The semi-quantitative elemental composition profile was obtained in depth by means of a line scan of the cross section of the TiO_x coatings using the energy dispersive X-ray spectroscopy (EDS) technique with an Oxford Instruments X-ray detector (Abingdon, United Kingdom) and AZtec software (Oxford Instruments, Abingdon, United Kingdom). Figure 3 shows the micrograph with the composition profile of Ti and O along the coating; the dark region on the right belongs to the Si substrate. The O content is very low at the interface with the Si substrate and rises towards the top surface of the coating. The Ti content is relatively constant along the TiO_x coatings.

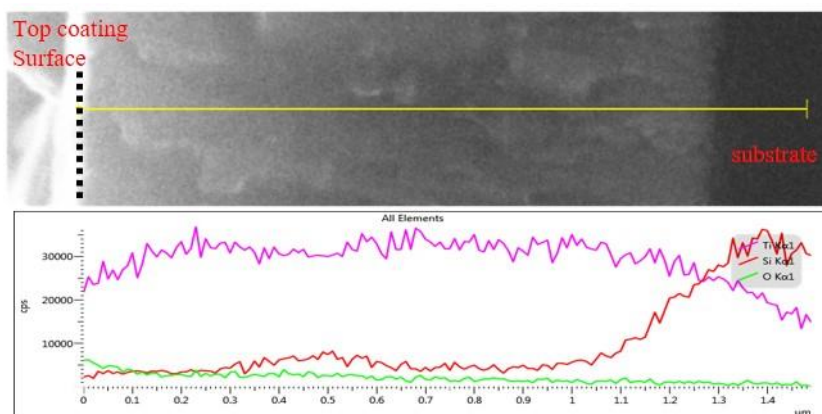


Figure 3. Linear elemental scan EDS analysis of the arc-PVD TiO_x coating.

2.1.4. EDS Mapping

The combination and superimposition of the EDS elemental maps on an informative electronic color image brings the benefits of automatic semi-qualitative analysis in two dimensions to identify the chemical elements and show their distributions in the PVD coatings as a function of the different Ar/ O_2 flow ratios. The chemical maps of the TiO_x coatings are shown in Figure 4a–c. The O K map in Figure 4c displays the major O content in the coating deposited using 300/100 Ar/ O_2 flow ratio. Further analysis was focused on this coating, this is considering that the plasma was stable enough during the deposition of the TiO_x with the 300/100 Ar/ O_2 flow ratio.

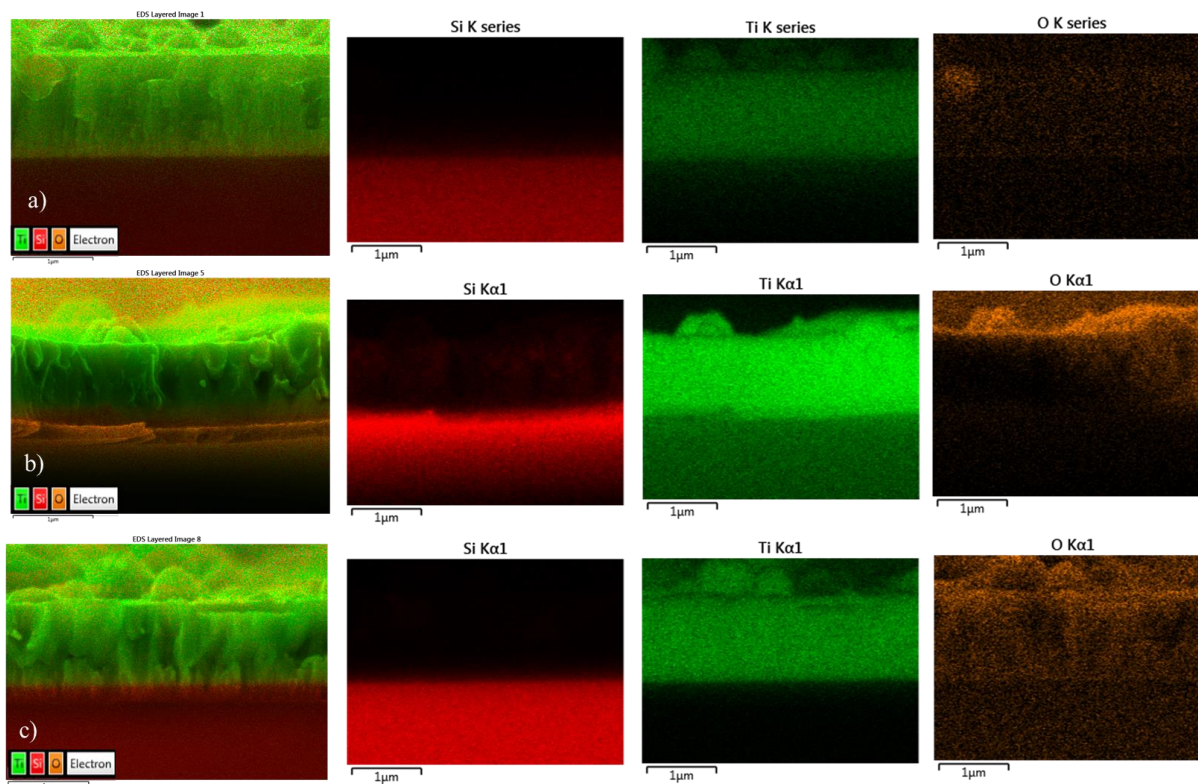


Figure 4. EDS mapping of the arc-PVD TiO_x coatings deposited with (a) 440 Ar/60 O_2 , (b) 400 Ar/100 O_2 , and (c) 300 Ar/100 O_2 .

2.1.5. EDS Spectra of the Coating with Fluxes of 300 Ar /100 O₂

Each EDS spectrum in Figure 5 indicates the content of the elements present at that position in the arc-PVD TiO_x coating. The spectrum 7 corresponds to the entire field of the SEM-image displayed in Figure 5.

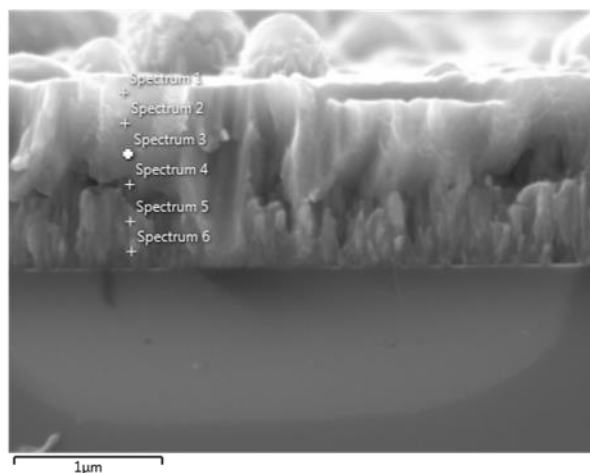


Figure 5. Micrograph showing the location of the EDS spectra from 1 to 6 in the TiO_x coating deposited using a 300/100 Ar/O₂ flow ratio.

The TiO_x coatings with Ar/O₂ flow ratios of 440/60 and 400/100 displayed relatively low O contents. The semi-quantitative elemental compositional analysis of the TiO_x coating using a 300 Ar/100 O₂ flow ratio is shown in Table 3. It is observed that the presence of Ti predominates in all the spectra. Important to remark is that the coating strategy considers the deposit of a thin Ti metallic bond layer at the interface with the borosilicate rings. This is not clearly demonstrated by the EDS analysis due to the thickness of Ti, which is expected to be only a few tens of nanometers. However, this is in agreement with the information indicating the presence of pure metallic Ti observed by the XRD evaluation discussed in the next section. At the top surface of the coating (spectrum 1) the concentration of Ti decreases, while the O concentration increases, so it is assumed that on the top layers of the graded coating the chemical composition will approach the formula TiO_x.

Table 3. Chemical composition estimated via the EDS spectra of TiO_x arc-PVD coatings deposited using 300/100 Ar/O₂ flow ratio.

Spectrum	% Weight		% Atomic	
	O	Ti	O	Ti
1	12.17	87.83	29.32	70.68
2	6.86	93.14	18.07	81.93
3	4.58	95.42	12.56	87.44
4	3.66	96.34	10.21	89.79
5	4.89	95.11	13.34	86.66
6	5.99	94.01	16.01	83.99
7	9.28	90.72	23.44	76.56

2.2. Characterization of Thin Film by PVD and Heat Treatment

2.2.1. X-ray Diffraction (XRD)

Only Ti metallic was identified in the TiO_x coatings in the as-coated state and for this reason a heat treatment at 500 °C/2 h in static lab air was carried out. Figure 6 shows the diffractograms of the TiO_x coatings deposited by applying different Ar/O₂ flow ratios and treated at 500 °C. The rutile TiO₂ phase is built upon this treatment, which is indexed by the ICDD File 01-078-1510. Pure Ti in α phase (ICDD File 00-044-1294) was also detected.

The peak at $\approx 70^\circ$ corresponds to the Si substrate. Since it was not possible to identify the phases present by XRD of normal incidence or Bragg–Brentano, we proceeded to perform XRD with grazing incidence to the PVD coatings with heat treatment at 500°C for 2 h on silicon plates.

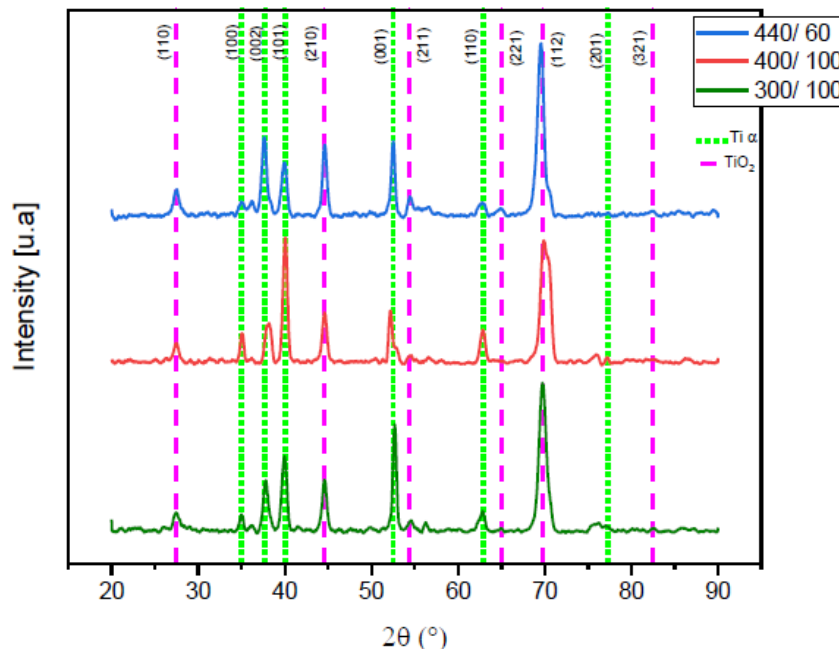


Figure 6. XRD diffractograms of heat-treated arc-PVD TiO_x coatings showing the characteristic peaks of hexagonal-Ti and rutile- TiO_2 .

2.2.2. Diffuse Reflectance

The UV-vis diffuse reflectance spectra of the PVD coatings on the Si plates with different flow ratios of Ar/O_2 and subjected to heat treatment at 500°C for 2 h are shown in Figure 7 where the absorption region for the 300 $\text{Ar}/100 \text{ O}_2$ coating ranges from 200 nm to 300 nm and high absorption from 300 nm to 800 nm in the visible region, for the 400 $\text{Ar}/100 \text{ O}_2$ coating the absorption region is from 200 nm to 400 nm and for the 440 $\text{Ar}/60 \text{ O}_2$ coating the absorption is observed in the region from 200 nm to ≈ 425 nm.

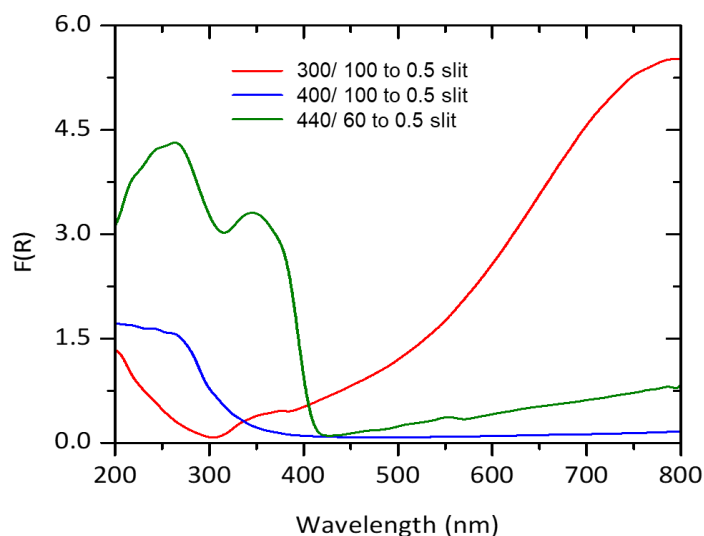


Figure 7. Kubelka–Munk absorbance function $F(R)$ vs. wavelength of the TiO_x arc-PVD coatings.

In order to correlate the reflectance spectrum to the energy band gap (E_g) of the TiO_x coatings, the Kubelka–Munk function was used. Then, to obtain the band gap, the Tauc's graphical procedure was applied, in which the Kubelka–Munk function and the photon energy, $h\nu$ expressed in eV, are related. This graph is shown in Figure 8, where the E_g is observed for each TiO_x coating obtained from the intersection of the tangent line with the horizontal axis.

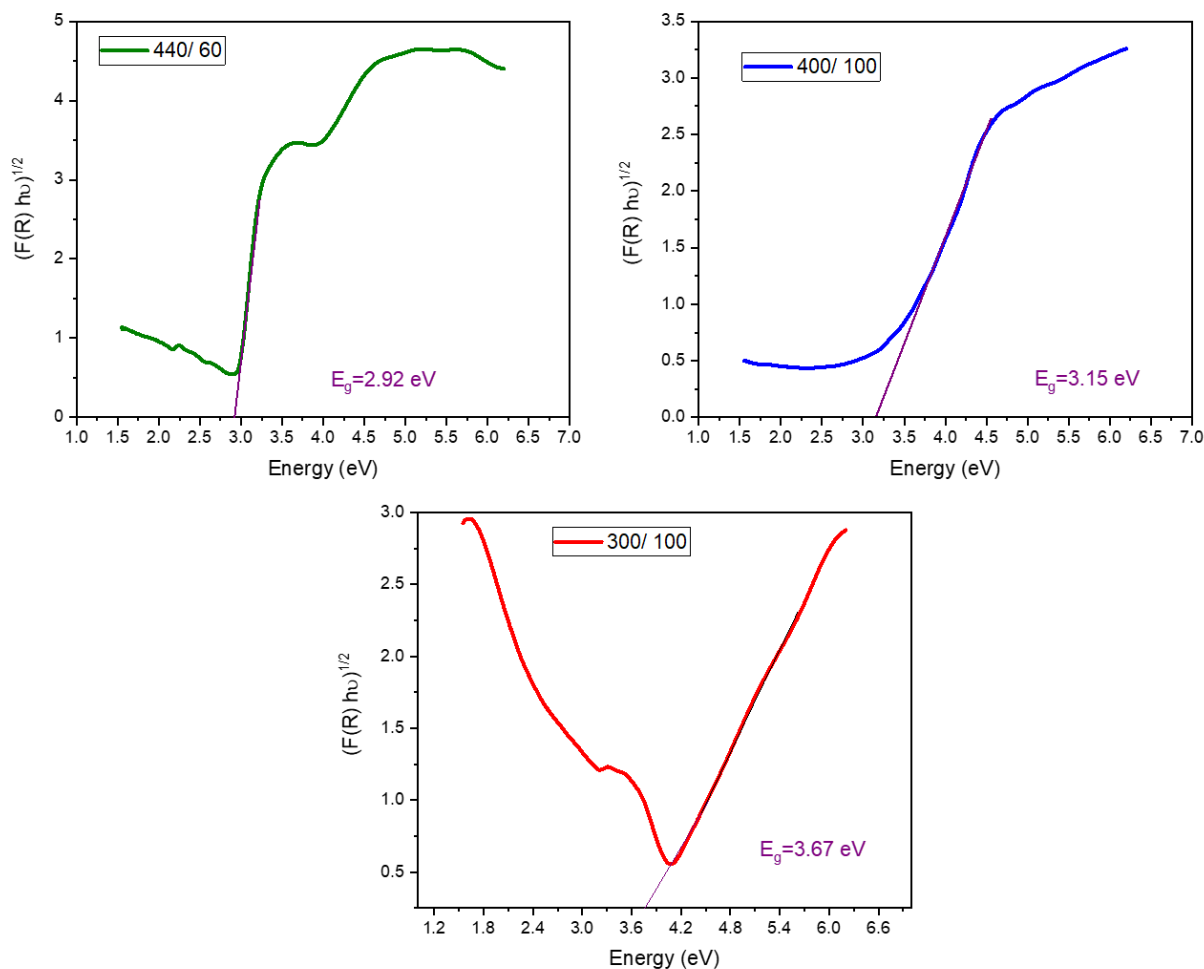


Figure 8. Tauc diagrams to calculate the E_g of the rings with argon-oxygen flow sccm 440–60, 400–100 and 300–100.

The E_g values of each coating indicate the energy required for the transfer of electrons from the valence band to the conduction band to take place. The E_g is related to the wavelength λ (nm) with the following equation:

$$E_g = \frac{hc}{\lambda} = \frac{1240}{\lambda} \quad (1)$$

where h is Planck's constant and c is the speed of light. From the above equation, it follows that the longer the wavelength of maximum absorption λ (nm), the narrower the bandgap E_g (eV).

The E_g of the coatings with 400 Ar/100 O_2 is 3.15 eV, corresponding to a maximum absorption wavelength of 394 nm, for 300 Ar/100 O_2 the E_g is 3.67 eV corresponding to 338 nm, so these films are expected to be activated under ultraviolet type A (UVA) radiation ranging from 315 nm to 400 nm, while the 440 Ar/60 O_2 coating its E_g is 2.92 eV, corresponding to 425 nm, and these are activated under visible light from 400 to 700 nm.

2.3. The Effect of Ag Deposited by Photo-Reduction on the TiO_x Arc-PVD Coatings

2.3.1. X-ray Diffraction (XRD)

Figure 9 shows the XRD diffractogram of the rings coated using this Ar/ O_2 flow ratio = 300/100 after undergoing the heat treatment and Ag photo-reduction. The XRD patterns are compared to the XRD data from Ag, Ti α , and 300/100 rings in relative intensity. The peak with the highest intensity, which is found at $\approx 38^\circ$, may belong to Ag and also the Ti α phase since it is a characteristic peak. The small diffraction peaks that are attributed to Ag with cubic structure (ICCD File 00-001-1167) prove the presence of Ag in the coated rings after photo-reduction.

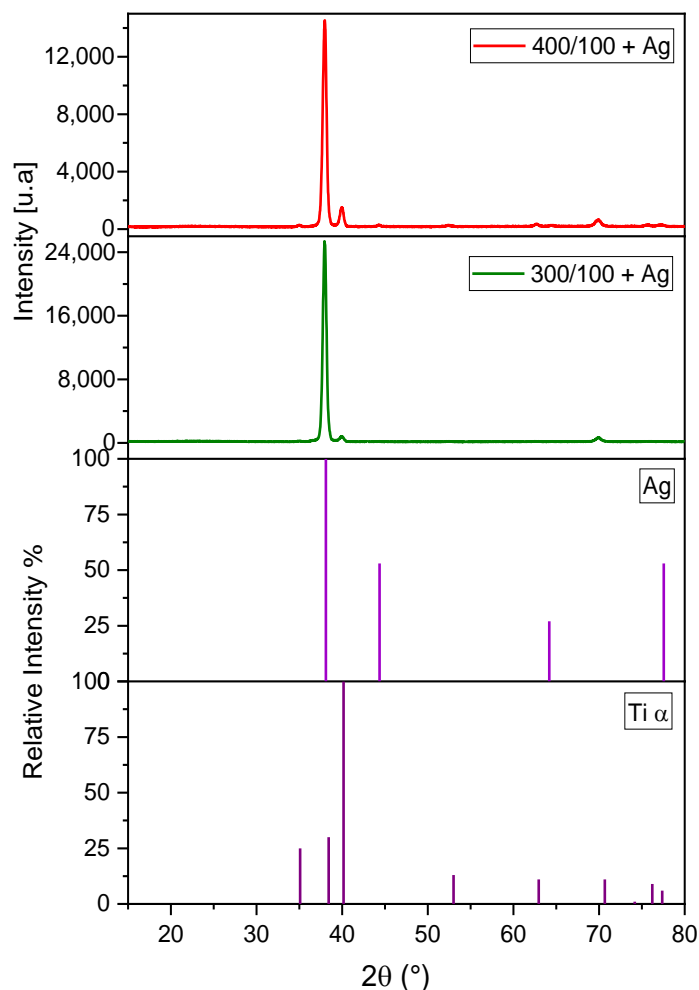


Figure 9. XRD diffractogram of the arc-PVD 400 Ar/100 O_2 and 300 Ar/100 O_2 TiO_x coating with heat treatment and photo-reduction of Ag with patterns in relative intensity of Ag and $\text{Ti}\alpha$.

2.3.2. Diffuse Reflectance

The UV-vis diffuse reflectance spectra of the TiO_x arc-PVD coatings deposited using different Ar/ O_2 flow ratios subjected to heat treatment and Ag photo-reduction are shown in Figure 10. The estimated absorption region for the 300 Ar/100 O_2 coating with Ag ranges from 350 nm to 800 nm and for the 400 Ar/100 O_2 coating with Ag are two absorption regions; the first one from 240 nm to 350 nm and the second of higher absorbance observed from 400 nm to 650 nm.

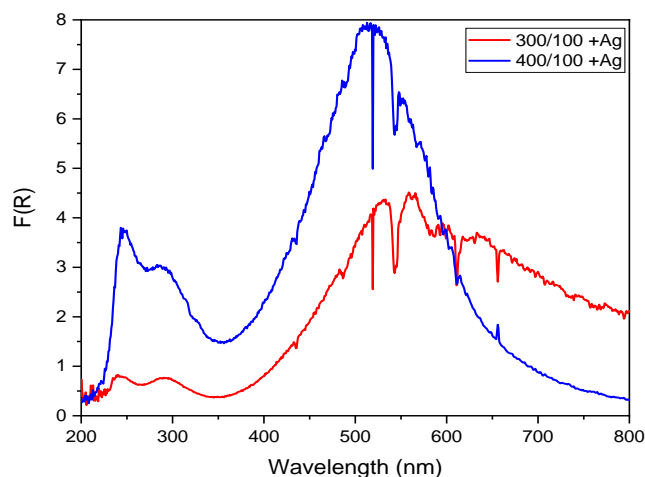


Figure 10. Kubelka–Munk absorbance function $F(R)$ vs wavelength for heat-treated TiO_x catalysts coated with Ag.

Figure 11 shows that the E_g for the 300 Ar/100 O_2 catalytic coating with Ag is 2.75 eV, corresponding to a maximum absorption wavelength of ≈ 451 nm, and for the 400 Ar/100 O_2 coatings with Ag its E_g is equal to 2.53 eV, corresponding to an absorption wavelength of 490 nm. The results indicate that the incorporation of silver in TiO_2 coatings caused a reduction in the E_g , which induced a shift towards the visible region for the photo-excitation of the catalytic Ag- TiO_2 surface. Therefore, an electronic transition from the Ag^+ energy levels to the Titania conduction band is considered to be the main reason for this reduction in the bandgap energy and the shift of the absorption response to the visible light region.

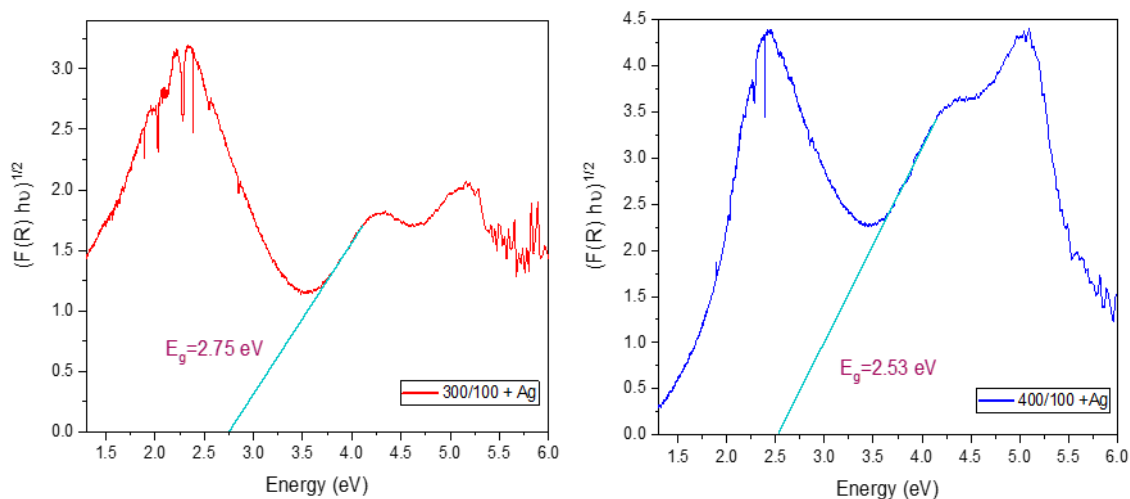


Figure 11. Tauc diagrams to calculate E_g of rings with TiO_x catalytic coatings deposited using Ar- O_2 flow ratio 300/100 and 400/100.

2.4. Degradation of Rhodamine B Dye by the Ag- TiO_x Photo-Catalysts

For catalytic testing, a reactor with a 2 l volume filled with 8 rings coated with Ag- TiO_x catalyst and a concentration of 0.5 ppm of rhodamine B was applied. The photo-catalyst Ag- TiO_x deposited with 400 Ar/100 O_2 degraded $\sim 68.18\%$, and the catalytic coating deposited with 300 Ar/100 O_2 decomposed $\sim 68.02\%$. The coated rings in the darkness showed no change in rhodamine B concentration over time, and the lamp on without the catalytic rings (photolysis) degraded only 15% of the dye. The amount of 0.066 g of TiO_2 in the anatase phase of the Sigma Aldrich (Burlington, MA, United States) brand in powder form, which

is equivalent to the mass of the coating of eight rings degraded 86% in a time of 75 min (Figure 12).

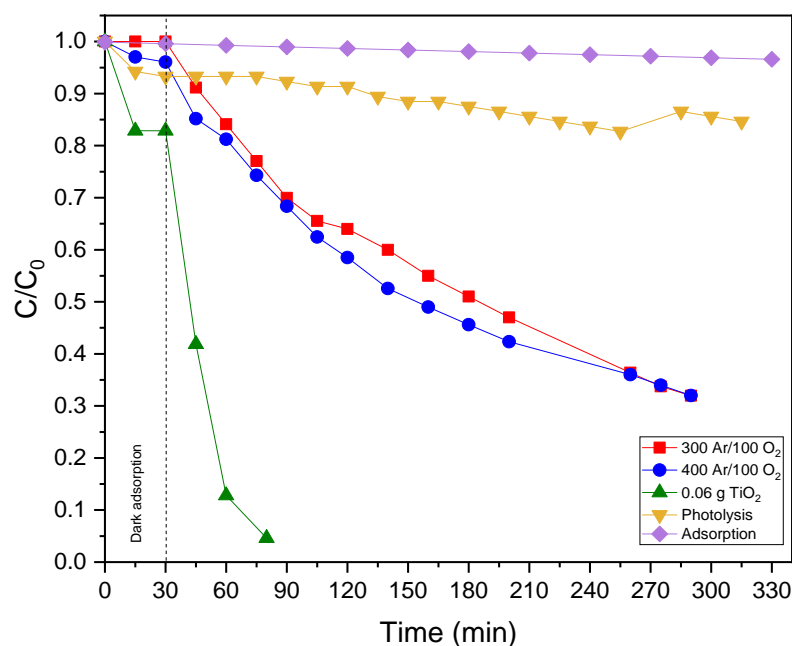


Figure 12. Change in rhodamine B concentration (2 L at 0.5 ppm RhB) with respect to time using different catalyst configurations. Arc-PVD Ag-TiO_x coating (circle and square), anatase-phase TiO₂ powder catalyst (triangle), photolysis (inverted triangle), and adsorption (rhomboid).

2.5. Determination of Reaction Kinetic Constants

To further explain the behavior of the rhodamine B degradation process, the kinetics of this reaction was determined with the experimental data presented in the last section. The criterion to calculate the reaction order was the one that best fit a straight line or that had the best linear correlation. In this sense, the degradation of rhodamine B fits the kinetics of a reaction with a pseudo first order. Table 4 shows the kinetic equations for this reaction, where C_0 is the initial dye concentration, C is the dye concentration at a given time, k_{ap} is the first order apparent rate constant, and t is the time in min.

Table 4. Kinetic parameters for rhodamine B degradation reaction.

Reaction Order	Reaction Speed (k_{ap})	Integration of k_{ap}	Line Graph to Determine k_{ap}	Half Life Time ($t_{1/2}$)
First order	$-\frac{d[C]}{dt} = k[C]$	$[C] = [C_0]e^{-kt}$	$\ln[C]$ vs t	$\frac{\ln(2)}{k}$

Table 5 shows the kinetic constants calculated for the Ag-TiO_x photo-catalyst deposited using 300/100 Ar/O₂ (0.0038 min⁻¹) and for the Ag-TiO_x photo-catalytic coating deposited using 400/100 Ar/O₂ (0.0041 min⁻¹). These reaction constants k_{ap} are still extremely low (~14.5 smaller) compared to the rhodamine degradation on the TiO₂ powder catalysts in suspension (0.0595 min⁻¹). Important to highlight is the specific surface area exposed in both catalytic systems. Catalysts in powder form offer great surface area, while PVD coatings are extremely dense with low specific surface areas. The advantages of fixed photo-catalysts would be the ease to separate the treated fluid from the solid catalyst.

Table 5. Kinetic data of the photo-catalytic degradation of rhodamine B over Ag-TiO_x catalyst deposited by arc-PVD.

Photocatalyst	C/C ₀	k _{ap} (min ⁻¹)	Half Life Time (t _{1/2}) (min)	R ²
TiO _x coating 400 Ar /100 O ₂	0.318	0.0041	169.06	0.9937
TiO _x coating 300 Ar/100 O ₂	0.319	0.0038	182.4	0.9951
Powder-TiO ₂	0.04	0.0595	11.64	0.9904

Kinetic constants of published results cannot be directly compared because they are all calculated using different reaction conditions, such as type of illumination, concentration of TiO₂ and rhodamine B, reactor design, catalyst immobilization method, and coating substrate. All these parameters are factors that have an effect on the kinetics of rhodamine degradation. For instance, [68] obtained a k_{ap} value of 0.00627 min⁻¹ in the degradation of rhodamine B on a TiO₂ catalyst supported on a porous ceramic substrate. This k_{ap} is 34.6% higher than the best k_{ap} obtained in the fixed supported Ag-TiO_x photo-catalyst discussed here.

2.6. Disinfection of Secondary Treatment Effluent by the Fixed Ag-TiO_x Photo-Catalysts

Two liters of water from the secondary treatment effluent of the GEA environmental treatment plant were used. The initial concentration varied since one experiment per day was carried out and the daily conditions of the treatment plant changed during its operation.

Table 6 shows that the initial and final concentrations of fecal coliforms in each experiment, as well as the percentage of elimination of fecal coliforms for eight rings coated with TiO_x using 300 Ar/100 O₂ coating was 83.69% equivalent to a logarithmic reduction of 0.79; similarly, the elimination of fecal coliforms on the TiO_x coating deposited using 400 Ar/100 O₂ was 90.32% equivalent to 1.01 Ulog reduction in 4 h with UV-A irradiation. A dark study was carried out to establish the effect of the immobilized catalyst as well as the reactor operating conditions on the viability of fecal coliforms. As can be observed, the bacterial concentration remained constant for 4 h. On the other hand, it is known that an adsorption effect can occur between the microorganism and catalyst (TiO₂) in suspension that favors microbial inactivation [69,70]. However, the results obtained show that there is no significant catalyst–microorganism adsorption phenomenon in the system, since the initial and final fecal coliform concentration after 4 h of treatment in darkness was similar.

Table 6. Concentration of fecal coliforms in NMP/100 mL and Ulog in secondary effluent water from the GEA Ambiental plant using Ag-TiO_x arc-PVD coatings on rings.

NMP/100 mL				
Ag-TiO _x Coatings				
Time	300 Ar/100 O ₂	400 Ar/100 O ₂	Photolysis	Rings in the dark
0	46,000	9300	400	400
4 h	7500	900	400	400
% removal	83.69	90.32	0	0
logarithmic units				
0	4.66	3.96	2.60	2.60
4 h	3.87	2.95	2.60	2.60
Ulog reduction	0.79	1.01	0	0

2.7. Disinfection of Synthetic Water by the Fixed Ag-TiO_x Photo-Catalysts

Synthetic water was used to analyze the bacterial elimination at high concentrations of fecal coliforms. In the disinfection experiments, a volume of 2 L during 4 h was selected. Table 7 shows that for eight coated rings with de TiO_x using 300 Ar/100 O₂, there was a percentage of elimination of fecal coliforms of 86% equivalent to 0.86 logarithmic reduction

units, for the TiO_x coating deposited using 400 Ar/100 O_2 of 78.18% or 0.66 Ulog reduction, while for photolysis and the rings in darkness there was no elimination at all.

Table 7. Concentration of fecal coliforms in NMP/100 mL and Ulog in synthetic water using Ag- TiO_x arc-PVD coatings on rings.

NMP/100 mL				
Ag- TiO_x Coatings				
Time	300 Ar/100 O_2	400 Ar/100 O_2	Photolysis	Rings in the dark
0	150,000	11,000,000	24,000,000	11,000,000
4 h	21,000	2,400,000	24,000,000	11,000,000
% removal	86	78.18	0	0
logarithmic units				
0	5.17	7.04	7.38	7.04
4 h	4.32	6.38	7.38	7.04
Ulog Reduction	0.85	0.66	0	0

3. Materials and Methods

3.1. Synthesis of Thin Films by PVD on Borosilicate Raschig Rings

Commercial borosilicate Raschig rings with $\text{Ø} = 10$ mm, length = 50 mm, and wall thickness = 1.5 mm were used as substrates for TiO_x deposition. First, the substrate rings were cleaned in an ultrasonic, using Elmasonic X-tra equipment (Singen, Germany) with an operating frequency of 45 KHz in ethanol for 15 min at room temperature. Then, they were dried and fixed in a 3-axis rotating planetary system for coating deposition, see left image in Figure 1. The rotating planetary system was introduced inside the coating chamber of the DOMINO mini semi-industrial equipment from OERLIKON (Bergisch Gladbach, Germany), where the TiO_x coating was deposited applying the cathodic arc method, see the coated Raschig rings in the middle and right images in Figure 13.



Figure 13. Raschig rings prepared for the PVD process (left), and substrates after arc-PVD TiO_x deposition (middle and right).

Firstly, the rings are heated at ~ 450 °C using a 9 kW heating system and applying a continuous vacuum. The heating provides cleaning by evaporating residual moisture from the surface of the borosilicate rings. Before the coating step, the rings' surface was cleaned with Ar^+ ions produced through the arc enhanced glow discharge (AEGD) process. During the coating of the TiO_x , a reaction takes place between the metallic Ti ions generated by erosion of the cathode material and the O ions. High purity gases are used for this process, oxygen (O_2) with a purity of 99.998%, and Ar with a purity of 99.999%. The Ar and O_2 flow rates were varied for each set of rings, and three sets of Ar/ O_2 ratios (440/60, 400/100, and 300/100) were selected and 11 Raschig rings were deposited during each coating run. The deposition time was maintained for 2 h by applying 80 V bias at a frequency of 20/80 KHz

and a current of 150 A. Lastly, the coated samples were cooled inside the PVD chamber for ~90 min.

The ring sets were characterized by field emission scanning electron microscopy (FE-SEM) for surface analysis, thickness, and morphology of the TiO_x films, X-ray energy dispersive spectrometry (EDS) for elemental analysis, and low angle X-ray diffraction (XRD) to identify crystalline phases in the coating. For this purpose, the XRD data were taken in a Rigaku diffractometer and by applying the parallel beam (PB) mode using $\text{Cu K}\alpha$ radiation with a wavelength of 1.540593 Å, angle $\omega = 1^\circ$, an angular range from 20° to 90° , and a step size of 0.02° .

3.2. Heat Treatment after PVD Coating

The Raschig rings coated with the TiO_x systems were heat-treated in a Thermo Scientific Lindberg Blue M furnace (Waltham, MA, USA) at 500°C for 2 h. Using a heating ramp of $10^\circ\text{C}/\text{min}$, this treatment was performed under standard conditions and air atmosphere. The heat treatment was performed in order to increase the O content on the surface of the coating according to [71,72]. Subsequently, the grazing incidence X-ray diffraction XRD method was applied to analyze the degree of oxidation and diffuse reflectance analysis was performed. Figure 14 shows the rings after heat treatment.



Figure 14. Raschig rings after heat treatment.

3.3. Doping of the TiO_x with Silver

Silver (Ag) was added to the TiO_x coating to activate it, and for this purpose, the photochemical reduction or photo-deposition methodology was applied, where the Ti/TiO_2 -coated rings were immersed twice for 5 min in a 1.7 wt. % AgNO_3 aqueous solution with CAS number 7761-88-8. Subsequently, they were irradiated with a UVC source ($\lambda = 254\text{ nm}$) for 2 h to activate the impregnated Ag [24,73]. X-ray diffraction (XRD) and diffuse reflectance analysis were performed after this doping process.

Ag, is used, which is the most promising metal, serving as a conduction band electron attractor, increasing the hole-electron separation, and facilitating electron excitation by the creation of a local electric field [74,75]. In this way, e^-/h^+ recombination is avoided. This property is due to the high reduction potential of the Ag^+ ion ($\text{Ag}^+ / \text{Ag}^0$) producing metallic Ag on the TiO_2 surface.

3.4. Dye Degradation Experiments

The photocatalytic activity of each set of rings coated with the Ag-doped TiO_2 was evaluated in the degradation of rhodamine B (RhB) with CAS number 81-88-9. Firstly, the calibration curve of the rhodamine B dye was performed, taking as reference the wavelength of maximum absorption of the dye of 554 nm. The photocatalytic degradation reactions were carried out in the photocatalytic reactor where its geometry corresponds to a cylinder 90 cm long, with a diameter of $3\frac{1}{2}$ " made of polyvinyl chloride (PVC) and with a stainless steel reflecting surface. Inside the reactor there is a 20 W TecnoLite F20T8BLB UV-A lamp of short wavelength between 315 and 400 nm, which is inside a quartz tube of

DExt = 3.2 cm, a wall thickness of 0.2 cm, and a length of 91.5 cm. The rings are attached to nylon threads from the top cover and are located in the free space between the quartz tube and the stainless steel surface, and the bottom is air inlet through an Elite 799 pump. The reactor operates in batch mode, with a volume of 2 l of a 0.5 ppm rhodamine B solution. In a typical photo-catalytic experiment, the aqueous solution was loaded into the reactor, left in the dark with stirring for 30 min to equilibrate, and then the UV-A lamp was turned on. Aliquots were taken at specific time intervals and analyzed using a BIOBASE BK-UV1800 spectrophotometer (Jinan, China). The obtained data were plotted to determine the reaction order. Subsequently, kinetic parameters, such as reaction rate, constant and half-life time, were calculated; this was done in order to evaluate the photo-catalytic efficiency of each set of TiO₂-coated rings. In the reaction system, the following experimental arrangement was carried out in the degradation of rhodamine B: (a) use of immobilized TiO₂ in the dark, (b) use of UV light lamp without immobilized TiO₂ "photolysis", (c) use of immobilized TiO₂ with UV light lamp "photocatalysis", and (d) degradation in the dark without catalyst.

3.5. Disinfection Experiments

The coated Ag-doped TiO₂ rings were evaluated in the elimination of fecal coliforms. For these, two water matrices were used: one from the secondary treatment effluent (before chlorination process) of the wastewater treatment plant of GEA Ambiental, Morelia, Mexico, and synthetic water prepared in the laboratory.

For the preparation of synthetic water, a sample was taken from the secondary treatment effluent of the GEA Ambiental plant and bacterial growth was performed in MacConkey broth medium. After incubation for 24–48 h at 35 °C, bacterial cells were transferred to 50 mL conical polypropylene centrifuge tubes with flat caps and collected by centrifugation at 4000 rpm for 5 min at room temperature. The supernatant was discarded and the sediment was resuspended in sterile phosphate solution or 0.9% NaCl normal saline. This solution is called microbial stock solution [76]. To obtain the synthetic water to be used in photocatalytic disinfection, ~ 20 mL of the microbial stock solution is resuspended in 2 L of sterile distilled water and mixed with magnetic stirring.

In a typical experiment, the inoculated aqueous solution was loaded into the reactor, left in the dark with stirring for 30 min to equilibrate, and then exposed to UV-A radiation. An aliquot was extracted at the beginning and end of the process, which was after 4 h. In order to evaluate the percentage of elimination of fecal coliforms, both aliquots were analyzed by means of the microbiological test of the most probable number in multiple tubes (MPN) for fecal coliforms following the Mexican standard NMX-AA-042-SCFI-2015.

The following tests are performed in the reactor in the elimination of fecal coliforms: (a) use of immobilized TiO₂ in darkness, (b) use of UV light lamp without immobilized TiO₂ "photolysis", (c) use of immobilized TiO₂ with UV light lamp "photocatalysis" and (d) degradation in the darkness without catalyst.

4. Conclusions

Heterogeneous photocatalysis stands out among advanced oxidation processes (AOPs) as a promising and effective biocidal technique, with titanium dioxide (TiO₂) being the most common catalyst employed for the purification of aqueous matrices. However, one of the main obstacles to putting it into practice is the separation of photocatalysts and the design of photocatalytic reactors, as most of the synthesized photocatalysts are in the form of powders. Alternatively, TiO₂ can be fixed on a solid support, eliminating the need to add a catalyst separation process. In this case, it should be noted that the process offers lower efficiencies due to the smaller surface area of catalysts exposed to light and molecules to be removed.

The Ag-TiO_x photocatalyst deposited with 400 Ar/100 O₂ degraded ~68.18%, and the catalytic coating deposited with 300 Ar/100 O₂ degraded ~68.02% of the rhodamine B dye at a concentration of 0.5 ppm in 2 L volume. In the disinfection, the TiO_x 300 Ar/100

O₂ coating had a fecal coliform removal of 83.69% and the TiO_x 400 Ar/100 O₂ coating removed 90.32%.

The results obtained cannot be directly compared with others because each of them used different reaction conditions, such as type of illumination, concentration of TiO₂ and rhodamine B, reactor design, catalyst immobilization method, and coating substrate. All these parameters are factors that have an effect on the kinetics of rhodamine B degradation and bacterial killing. However, they are positive results on rhodamine B degradation for TiO_x-Ag thin films if the results obtained for TiO₂-Ag thin films synthesized with a sol-gel method deposited by dip coating on the Ag substrates and photo-chemical deposition shown in Table 1 are known.

1. Targeting the application of fixed photo-catalysts, TiO_x coatings were deposited by cathodic arc physical vapor deposition on borosilicate Raschig rings. The deposit was designed for O grading using flow ratios of 440 Ar/60 O₂, 400 Ar/100 O₂, and 300 Ar/100 O₂ in a semi-industrial coater unit. The arc-PVD plasma was stable in all Ar/O₂ mixtures.
2. In the as-coated state, the TiO_x catalysts are composed of pure Ti in the α phases. The EDS analysis showed that O and Ti varies in the depth of the coating, suggesting the formation of a system with a low amount of O producing a nonstoichiometric oxide (TiO_x). A heat treatment was needed in order to increase the amount of O in the coating and build the crystalline TiO₂ rutile phase.
3. After the thermal treatment, the analysis by UV vis diffuse reflectance spectroscopy indicated that the TiO_x catalytic coatings using 400 Ar/100 O₂ and 300 Ar/100 O₂ are activated under UVA radiation, while the coating 440 Ar/60 O₂ absorbs in the visible spectrum.
4. Silver, confirmed by XRD, was added by the UVC photo-reduction method in the TiO_x photo-catalysts deposited using 400 Ar/100 O₂ and 300 Ar/100 O₂ sccm sets. In this Ag-TiO_x photo-catalyst, a decrease in the bandgap energy was observed, thus showing moderate photo-catalytic activity in the degradation of rhodamine B at 0.5 ppm and the removal of fecal coliforms from a secondary treatment effluent and synthetic water.

Author Contributions: Conceptualization, F.U.-M., G.C.M.-R. and R.H.-A.; investigation, A.Y.R.-T.; resources, E.M.R.-M. and F.J.M.; writing—original draft preparation, A.Y.R.-T.; writing—review and editing, R.H.-A. and G.C.M.-R.; visualization, G.C.M.-R.; supervision, J.A.-C.; funding acquisition, R.H.-A. All authors have read and agreed to the published version of the manuscript.

Funding: Financial resources and materials were partially provided through the FORDECYT/247/2018 project 297265 (Fortalecimiento de las Capacidades de Investigación, Desarrollo e Innovación del CIDESI para Atender las Necesidades Científico-Tecnológicas en Manufactura Aditiva de la Industria en la Región Centro-Norte de México), FORDECYT 296384 (Operación de consorcio CONACYT en manufactura aditiva), and the 2015-02-1077 (Estudio y Entendimiento de la Degradación y Estabilidad de Sistemas de Recubrimientos Duros Lubricantes para Aplicaciones de Mediana y Alta Temperatura) Frontiers of Science program managed by CONACYT. Dr. R. Huirache-Acuña thanks to CIC 2022 UMSNH Project.

Acknowledgments: The authors thank the access provided to the PVD coater unit and characterization equipment of the National Lab.- CENAPROT in CIDESI-Querétaro. G.C. Mondragón-Rodríguez, thank the Investigadoras e Investigadores por México program (previously Cátedras-CONACYT) sponsored by CONACYT. Thanks to J. Martín Yañez Limón for facilitating the access to the UV-vis equipment at CINVESTAV in Querétaro, Mexico. R. Huirache-Acuña thanks to B. Millán-Malo and C. Peza-Ledesma from CFATA-UNAM for their XRD Technical support.

Conflicts of Interest: The authors declare no conflict of interest.

References

1. Naffouti, W.; Nasr, T.B.; Mehdi, A.; Kamoun-Turki, N. Effect of sprayed solution flow rate on the physical properties of anatase TiO₂ thin films. *J. Electron. Mater.* **2014**, *43*, 4033–4040. [[CrossRef](#)]
2. Giordano, F.; Abate, A.; Correa, J.P.; Saliba, M.; Matsui, T.; Im, S.H.; Graetzel, M. Enhanced electronic properties in mesoporous TiO₂ via lithium doping for high-efficiency perovskite solar cells. *Nat. Commun.* **2016**, *7*, 10379. [[CrossRef](#)] [[PubMed](#)]
3. Park, J.; Jin, T.; Liu, C.; Li, G.; Yan, M. Three-Dimensional Graphene-TiO₂ Nanocomposite Photocatalyst Synthesized by Covalent Attachment. *ACS Omega* **2016**, *1*, 351–356. [[CrossRef](#)]
4. Rane, S.S.; Kajale, D.A.; Arbuj, S.S.; Rane, S.B.; Gosavi, S.W. Hydrogen, ethanol and ammonia gas sensing properties of nano-structured titanium dioxide thick films. *J. Mater. Sci. Mater. Electron.* **2017**, *28*, 9011–9016. [[CrossRef](#)]
5. Lanin, S.N.; Vlasenko, E.V.; Kovaleva, N.V.; Zung, F.T. The adsorption properties of titanium dioxide. *Russ. J. Phys. Chem.* **2008**, *82*, 2152–2155. [[CrossRef](#)]
6. Nunes, D.; Fortunato, E.; Martins, R. Flexible nanostructured TiO₂-based gas and UV sensors: A review. *Discov. Mater.* **2022**, *2*, 2. [[CrossRef](#)]
7. Ding, S.N.; Gao, B.H.; Shan, D.; Sun, Y.M.; Cosnier, S. TiO₂ nanocrystals electrochemiluminescence quenching by biological enlarged nanogold particles and its application for biosensing. *Biosens. Bioelectron.* **2013**, *39*, 342–345. [[CrossRef](#)]
8. Mun, K.S.; Alvarez, S.D.; Choi, W.Y.; Sailor, M.J. A stable, label-free optical interferometric biosensor based on TiO₂ Nanotube Arrays. *ACS Nano* **2010**, *4*, 2070–2076. [[CrossRef](#)]
9. Hou, Z.; Zhang, Y.; Deng, K.; Chen, Y.; Li, X.; Deng, X.; Cheng, Z.; Lian, H.; Li, C.; Lin, J. UV-emitting upconversion-based TiO₂ photosensitizing nanoplatform: Near-infrared light mediated in vivo photodynamic therapy via mitochondria-involved apoptosis pathway. *ACS Nano* **2015**, *9*, 2584–2599. [[CrossRef](#)]
10. Deepagan, V.G.; You, D.G.; Um, W.; Ko, H.; Kwon, S.; Choi, K.Y.; Yi, G.R.; Lee, J.Y.; Lee, D.S.; Kim, K.; et al. Long-Circulating Au-TiO₂ Nanocomposite as a Sonosensitizer for ROS-Mediated Eradication of Cancer. *Nano Lett.* **2016**, *16*, 6257–6264. [[CrossRef](#)]
11. Chinnamuthu, P.; Dhar, J.C.; Mondal, A.; Bhattacharyya, A.; Singh, N.K. Ultraviolet detection using TiO₂ nanowire array with Ag Schottky contact. *J. Phys. D Appl. Phys.* **2012**, *45*, 135102–135105. [[CrossRef](#)]
12. Zhang, H.; Ruan, S.; Li, H.; Zhang, M.; Lv, K.; Feng, C.; Chen, W. Schottky diode ultraviolet detector based on TiO₂ nanowire array. *IEEE Electron. Device Lett.* **2012**, *33*, 83–85. [[CrossRef](#)]
13. Yu, H.; Chen, J.; Wang, W.; Dai, Q. Optical waveguide lightmode spectroscopy (OWLS) as a sensor for thin film and quantum dot corrosion. *Sensors* **2012**, *12*, 17330–17342. [[CrossRef](#)]
14. Wang, D.; Li, X.; Chen, J.; Tao, X. Enhanced photoelectrocatalytic activity of reduced graphene oxide/TiO₂ composite films for dye degradation. *Chem. Eng. J.* **2012**, *198*, 547–554. [[CrossRef](#)]
15. O'Regan, B.; Grätzel, M. A low-cost, high-efficiency solar cell based on dye-sensitized colloidal TiO₂ films. *Nature* **1991**, *353*, 737–740. [[CrossRef](#)]
16. Morozova, M.; Kluson, P.; Krysa, J.; Zlamal, M.; Solcova, O.; Kment, S.; Steck, T. Role of the template molecular structure on the photo-electrochemical functionality of the sol-gel titania thin films. *J. Sol-Gel Sci. Technol.* **2009**, *52*, 398–407. [[CrossRef](#)]
17. Kment, S.; Hubicka, Z.; Kmentova, H.; Kluson, P.; Krysa, J.; Gregora, I.; Morozova, M.; Cada, M.; Petras, D.; Dytrych, P.; et al. Photoelectrochemical properties of hierarchical nanocomposite structure: Carbon nanofibers/TiO₂/ZnO thin films. *Catal. Today* **2011**, *161*, 8–14. [[CrossRef](#)]
18. Kment, S.; Kluson, P.; Hubicka, Z.; Krysa, J.; Cada, M.; Gregora, I.; Deyneka, A.; Remes, Z.; Zabova, H.; Jastrabik, L. Double hollow cathode plasma jet-low temperature method for the TiO₂-xNx photoresponding films. *Electrochim. Acta* **2010**, *55*, 1548–1556. [[CrossRef](#)]
19. Kment, S.; Kluson, P.; Bartkova, H.; Krysa, J.; Churpita, O.; Cada, M.; Virostko, P.; Kohout, M.; Hubicka, Z. Advanced methods for titanium (IV) oxide thin functional coatings. *Surf. Coat. Technol.* **2008**, *202*, 2379–2383. [[CrossRef](#)]
20. Karuppuchamy, S.; Nonomura, K.; Yoshida, T.; Sugiura, T.; Minoura, H. Cathodic electrodeposition of oxide semiconductor thin films and their application to dye-sensitized solar cells. *Solid State Ion.* **2002**, *151*, 19–27. [[CrossRef](#)]
21. Djošić, M.; Mišković-Stanković, V.; Janačković, D.T.; Kačarević-Popović, Z.; Petrović, R. Electrophoretic deposition and characterization of boehmite coatings on titanium substrate. *Colloids Surf.* **2006**, *274*, 185–191. [[CrossRef](#)]
22. Liu, S.; Chen, X. Preparation and characterization of a novel activated carbon-supported N-doped visible light response photocatalyst (TiO₂ - xNy/AC). *J. Chem. Technol. Biotechnol.* **2007**, *82*, 453–459. [[CrossRef](#)]
23. Okada, K.; Takamatsu, Y.; Tokudome, Y.; Nakahira, A.; Takahashi, M. Highly oriented growth of titanate nanotubes (TNTs) in micro and confinement spaces on sol-gel derived amorphous TiO₂ thin films under moderate hydrothermal condition. *J. Sol-Gel Sci. Technol.* **2013**, *65*, 36–40. [[CrossRef](#)]
24. Kment, S.; Kmentova, H.; Hubicka, Z.; Olejnicek, J.; Cada, M.; Krysa, J. Enhanced photocatalytic activity of silver-doped nanoparticulate TiO₂ thin films with respect to the method of doping. *Res. Chem. Intermed.* **2015**, *41*, 9343–9355. [[CrossRef](#)]
25. Muaz, A.K.M.; Hashim, U.; Ibrahim, F.; Thong, K.L.; Mohktar, M.S.; Liu, W.W. Effect of annealing temperatures on the morphology, optical and electrical properties of TiO₂ thin films synthesized by the sol-gel method and deposited on Al/TiO₂/SiO₂/p-Si. *Microsyst. Technol.* **2016**, *22*, 871–881. [[CrossRef](#)]
26. Chen, Y.; Wang, K.; Lou, L. Photodegradation of dye pollutants on silica gel supported TiO₂ particles under visible light irradiation. *J. Photochem. Photobiol.* **2004**, *163*, 281–287. [[CrossRef](#)]

27. Tonejc, A.M.; Turković, A.; Gotić, M.; Musić, S.; Vuković, M.; Trojko, R.; Tonejc, A. HREM, TEM and XRD observation of nanocrystalline phases in TiO₂ obtained by the sol-gel method. *Mater. Lett.* **1997**, *31*, 127–131. [[CrossRef](#)]
28. Kavaliunas, V.; Sestakauskaite, A.; Sriubas, M.; Laukaitis, G. Influence of Deposition Parameters on the Structure of TiO Thin Films Prepared by Reactive Magnetron Sputtering Technique. *Lect. Notes Netw. Syst.* **2019**, *53*, 49–57. [[CrossRef](#)]
29. Sobrinho, V.S.S.; Neto, J.Q.M.; Lima, L.L.F.; Souza, I.A.; Libório, M.S.; Queiroz, J.C.A.; Sousa, R.R.M.; Almeida, E.O.; Feitor, M.C.; Costa, T.H.C. Optical-Electrical Properties and Thickness Analysis of TiO₂ Thin Films Obtained by Magnetron Sputtering. *Braz. J. Phys.* **2020**, *50*, 771–779. [[CrossRef](#)]
30. Horprathum, M.; Eiamchai, P.; Chindaudom, P.; Pokaipisit, A.; Limsuwan, P. Oxygen partial pressure dependence of the properties of TiO₂ thin films deposited by DC reactive magnetron sputtering. *Procedia Eng.* **2012**, *32*, 676–682. [[CrossRef](#)]
31. Guo, D.; Ito, A.; Goto, T.; Tu, R.; Wang, C.; Shen, Q.; Zhang, L. Preparation of rutile TiO₂ thin films by laser chemical vapor deposition method. *J. Adv. Ceram.* **2013**, *2*, 162–166. [[CrossRef](#)]
32. Wang, S.; Wang, K.; Jehng, J.; Liu, L. Preparation of TiO₂/MCM-41 by plasma enhanced chemical vapor deposition method and its photocatalytic activity. *Front. Environ. Sci. Eng.* **2011**, *6*, 304–312. [[CrossRef](#)]
33. Naffouti, W.; Jrad, A.; Nasr, T.B.; Ammar, S.; Turki-Kamoun, N. Structural, morphological and optical properties of TiO₂: Mn thin films prepared by spray pyrolysis technique. *J. Mater. Sci. Mater. Electron.* **2016**, *27*, 4622–4630. [[CrossRef](#)]
34. Doubi, Y.; Hartiti, B.; Labrim, H.; Fadili, S.; Tahri, M.; Belafhaili, A.; Siadat, M.; Thevenin, P. Experimental study of properties of TiO₂ thin films deposited by spray pyrolysis for future sensory applications. *Appl. Phys. A* **2021**, *127*, 475. [[CrossRef](#)]
35. Lahiri, R.; Ghosh, A.; Dwivedi, S.M.M.D.; Chakrabarty, S.; Chinnamuthu, P.; Mondal, A. Performance of Erbium-doped TiO₂ thin film grown by physical vapor deposition technique. *Appl. Phys. A Mater. Sci. Processing* **2017**, *123*, 573. [[CrossRef](#)]
36. Shubham, K.; Chakrabarti, P. Fabrication and characterization of metal/insulator/semiconductor structures based on TiO₂ and TiO₂/SiO₂ thin films prepared by low-temperature arc vapor deposition. *Electron. Mater. Lett.* **2014**, *10*, 579–584. [[CrossRef](#)]
37. Yap, Y.K.; Zhang, D. Physical Vapor Deposition. In *Encyclopedia of Nanotechnology*; Bhushan, B., Ed.; Springer: Dordrech, The Netherlands, 2015; pp. 1–8. [[CrossRef](#)]
38. György, G.; Socol, E.; Axente, I.N.; Mihailescu, C.; Ducu, C.; Ciuca, S. Anatase phase TiO₂ thin films obtained by pulsed laser deposition for gas sensing applications. *Appl. Surf. Sci.* **2005**, *247*, 429–433. [[CrossRef](#)]
39. Brunella, M.; Diamanti, M.; Pedefferri, M.; Fonzo, F.; Casari, C.; Bassi, A. Photocatalytic behavior of different titanium dioxide layers. *Thin Solid Film.* **2007**, *515*, 6309–6313. [[CrossRef](#)]
40. Sahm, H.; Zywitzki, O.; Glöß, D.; Modes, T.; Frach, P.; Goedicke, K. Structure and properties of crystalline titanium oxide layers deposited by reactive pulse magnetron sputtering. *Surf. Coat. Technol.* **2004**, *180*, 538–543.
41. Heo, C.; Lee, S.; Boo, J. Deposition of TiO₂ thin films using RF magnetron sputtering method and study of their surface characteristics. *Thin Solid Film.* **2005**, *475*, 183–188. [[CrossRef](#)]
42. Zhang, F.; Wang, X.; Li, C.; Wang, H.; Chen, L.; Liu, X. Rutile-type titanium oxide films synthesized by filtered arc deposition. *Surf. Coat. Technol.* **1998**, *110*, 136–139. [[CrossRef](#)]
43. Takikawa, H.; Matsui, T.; Sakakibara, A.; Bendavid, A.; Martin, P. Properties of titanium oxide film prepared by reactive cathodic vacuum arc deposition. *Thin Solid Film.* **1999**, *348*, 145–151. [[CrossRef](#)]
44. Attenberger, W.; Thorwarth, G.; Manova, D.; Mändl, S.; Stritzker, B.; Rauschenbach, B. Interface properties of TiO₂ on Si formed by simultaneous implantation and deposition of titanium and oxygen ions. *Surf. Coat. Technol.* **2001**, *142*, 412–417. [[CrossRef](#)]
45. Leng, Y.X.; Chen, J.Y.; Sun, H.; Yang, P.; Wan, G.J.; Wang, J.; Huang, N. Properties of titanium oxide synthesized by pulsed metal vacuum arc deposition. *Surf. Coat. Technol.* **2004**, *176*, 141–147. [[CrossRef](#)]
46. Zheng, P.; Wu, H.; Guo, J.; Dong, J.; Jia, S.; Zhu, Z. P–N co-doping induced structural recovery of TiO₂ for overall water splitting under visible light irradiation. *J. Alloy. Compd.* **2014**, *615*, 79–83. [[CrossRef](#)]
47. Noguez, C. Surface Plasmons on Metal Nanoparticles: The Influence of Shape and Physical Environment. *J. Phys. Chem. C* **2007**, *111*, 3606–3619. [[CrossRef](#)]
48. Trabelsi, K.; Hajjaji, A.; Ka, I.; Gaidi, M.; Bessais, B.; el Khakani, M.A. Optoelectronic and photocatalytic properties of in situ platinum-doped TiO₂ films deposited by means of pulsed laser ablation technique. *J. Mater. Sci. Mater. Electron.* **2017**, *28*, 3317–3324. [[CrossRef](#)]
49. Hassan, A.; Kayani, Z.N.; Anwar, M. Effect of Au ions on structural, optical, magnetic, dielectric, and antibacterial properties of TiO₂ dip-coated thin films. *J. Mater. Sci. Mater. Electron.* **2021**, *32*, 14398–14419. [[CrossRef](#)]
50. Khan, S.; ul Haq, M.; Ma, Y.; Nisar, M.; Li, Y.; Khan, R.; Han, G.; Liu, Y. Structural and optical properties of macroporous Ag@TiO₂ thin films prepared by a facile one-step sol–gel method. *J. Sol-Gel Sci. Technol.* **2019**, *93*, 273–280. [[CrossRef](#)]
51. Heiba, Z.K.; Mohamed, M.B.; Badawi, A. Structural and Optical Characteristic of Cu-Doped TiO₂ Thin Film. *J. Inorg. Organomet. Polym. Mater.* **2022**, *32*, 2853–2862. [[CrossRef](#)]
52. Balakrishnan, A.; Appunni, S.; Chinthala, M.; Vo, D.V.N. Biopolymer-supported TiO₂ as a sustainable photocatalyst for wastewater treatment: A review. *Environ. Chem. Lett.* **2022**, *3*, 1–28. [[CrossRef](#)]
53. Obregón, S.; Rodríguez-González, V. Photocatalytic TiO₂ thin films and coatings prepared by sol–gel processing: A brief review. *J. Sol-Gel Sci. Technol.* **2021**, *102*, 125–141. [[CrossRef](#)]
54. ACLAC. Economic Commission for Latin America and the Caribbean. 2004. Available online: <https://observatoriop10.cepal.org/es/tratados/convenio-estocolmo-contaminantes-organicos-persistentes> (accessed on 3 March 2022).

55. Anjaneyulu, R.B.; Mohan, B.S.; Naidu, G.P.; Muralikrishna, R. Visible light enhanced photocatalytic degradation of methylene blue by ternary nanocomposite, MoO₃/Fe₂O₃/rGO. *J. Asian Ceram. Soc.* **2018**, *6*, 183–195. [[CrossRef](#)]
56. Klut, M.E.; Bisalputra, T.; Antia, N.J. The use of fluorochromes in the cytochemical characterization of some phytoflagellates. *Histochem. J.* **1988**, *20*, 35–40. [[CrossRef](#)] [[PubMed](#)]
57. Rani, S.A.; Pitts, B.; Stewart, P.S. Rapid Diffusion of Fluorescent Tracers into Staphylococcus epidermidis Biofilms Visualized by Time Lapse Microscopy. *Antimicrob. Agents Chemother.* **2005**, *49*, 728–732. [[CrossRef](#)] [[PubMed](#)]
58. Rinne, W.E.; Deacon, J.E. Fluorescent Pigment and Immersion Stain Marking Techniques for Lepidomeda mollispinis and Cyprinodon nevadensis. *Trans. Am. Fish. Soc.* **1973**, *102*, 459–462. [[CrossRef](#)]
59. Sagoo, S.K.; Jockusch, R.A. The fluorescence properties of cationic rhodamine B in the gas phase. *J. Photochem. Photobiol. A Chem.* **2011**, *220*, 173–178. [[CrossRef](#)]
60. Wilhelm, P.; Stephan, D. Photodegradation of rhodamine B in aqueous solution via SiO₂@TiO₂ nano-spheres. *J. Photochem. Photobiol. A Chem.* **2007**, *185*, 19–25. [[CrossRef](#)]
61. Zhao, X.; Zhu, Y. Synergetic Degradation of Rhodamine B at a Porous ZnWO₄ Film Electrode by Combined Electro-Oxidation and Photocatalysis. *Environ. Sci. Technol.* **2006**, *40*, 3367–3372. [[CrossRef](#)]
62. Mahmood, M.A.; Baruah, S.; Anal, A.K.; Dutta, J. Microbial Pathogen Inactivation Using Heterogeneous Photocatalysis. In *Environmental Chemistry for a Sustainable World*; Springer: Dordrecht, The Netherlands, 2012; pp. 511–541.
63. Hossain, M.A.; Elias, M.; Sarker, D.R.; Diba, Z.R.; Mithun, J.M.; Azad, M.A.K.; Siddiquey, I.A.; Rahman, M.M.; Uddin, J.; Uddin, M. Synthesis of Fe- or Ag-doped TiO₂-MWCNT nanocomposite thin films and their visible-light-induced catalysis of dye degradation and antibacterial activity. *Res. Chem. Intermed.* **2018**, *44*, 2667–2683. [[CrossRef](#)]
64. Hou, X.; Wu, X.; Liu, A. Studies on photocatalytic activity of Ag/TiO₂ films. *Front. Chem. China* **2006**, *1*, 402–407. [[CrossRef](#)]
65. Kader, S.; Al-Mamun, M.R.; Suhan, M.B.K.; Shuchi, S.B.; Islam, M.S. Enhanced photodegradation of methyl orange dye under UV irradiation using MoO₃ and Ag doped TiO₂ photocatalysts. *Environ. Technol. Innov.* **2022**, *27*, 102476. [[CrossRef](#)]
66. Wang, X.; Hou, X.; Luan, W.; Li, D.; Yao, K. The antibacterial and hydrophilic properties of silver-doped TiO₂ thin films using sol-gel method. *Appl. Surf. Sci.* **2012**, *258*, 8241–8246. [[CrossRef](#)]
67. Molina-Reyes, J.; Romero-Morán, A.; Sánchez-Salas, J.L. Enhanced photocatalytic bacterial inactivation of atomic-layer deposited anatase-TiO₂ thin films on rutile-TiO₂ nanotubes. *Photochem. Photobiol. Sci.* **2020**, *19*, 399–405. [[CrossRef](#)]
68. Araujo-Scharnber, A. Porous ceramic supported TiO₂ nanoparticles: Enhanced photocatalytic activity for rhodamine B degradation. *Bol. Soc. Esp. Cerám. Vidr.* **2020**, *59*, 230–238. [[CrossRef](#)]
69. Polo-Lopez, M.I.; Fernandez-Ibañez, P.; Garcia-Fernandez, I.; Oller, I.; Salgado-Trnsito, I.; Sichel, C. Resistance of *Fusarium sp* spores to solar TiO₂ photocatalysis: Influence of spore type and water. *Scaling-Up Results* **2010**, *85*, 1038–1048.
70. Sichel, C.; Blanco, J.; Malato, S.; Fernández-Ibañez, P. Effects of experimental conditions on *E. coli* survival during solar photocatalytic water disinfection. *J. Photochem. Photobiol. A Chem.* **2007**, *189*, 239–246. [[CrossRef](#)]
71. Christensen, P.; Curtis, T.; Egerton, T.; Kosa, S.; Tinlin, J. Photoelectrocatalytic and photocatalytic disinfection of *E. coli* suspensions by titanium dioxide. *Applied Catal. B Environ.* **2003**, *41*, 371–386. [[CrossRef](#)]
72. Lopes, P.; Montagnoli, R.; Bidoia, E. Photocatalytic Degradation of phenol by thermal titanium dioxide thin layer electrodes. *Water Air Soil Pollut.* **2012**, *223*, 3673–3688. [[CrossRef](#)]
73. Santos, A. *Water Disinfection by Photocatalytic Process Using Titanium Dioxide Thermal Electrodes for Inactivation of Escherichia Coli and Staphylococcus aureus*; Bioscience Institute; UNESP—Univ Estadual Paulista: Rio Claro, Brazil, 2008.
74. Zhao, G.; Kozuka, H.; Yoko, T. Sol-gel preparation and photoelectrochemical properties of TiO₂ films containing Au and Ag metal particles. *Thin Solid Films* **1996**, *277*, 147–154. [[CrossRef](#)]
75. Herrmann, J.M.; Tahiri, H.; Ait-Ichou, Y.; Lassaletta, G.; Gonzalez-Elipse, A.R.; Fernandez, A. Characterization and photocatalytic activity in aqueous medium of TiO₂ and Ag-TiO₂ coatings on quartz. *Appl. Catal. B Environ.* **1997**, *13*, 219–228. [[CrossRef](#)]
76. Zarei, M.; Jamnejad, A.; Khajehali, E. Antibacterial effect of silver nanoparticles against four foodborne pathogens. *Jundishapur J. Microbiol.* **2014**, *7*, e8720. [[CrossRef](#)] [[PubMed](#)]